How textural features can improve SAR-based tropical forest disturbance mapping

Johannes Balling [a,*], Martin Herold [a,b], Johannes Reiche [a]

[a] *Wageningen University, Laboratory of Geo-Information Science and Remote Sensing, Wageningen, the Netherlands*
[b] *Helmholtz GFZ German Research Centre for Geosciences, Remote Sensing and Geoinformatics, Potsdam, Germany*

A R T I C L E I N F O

A B S T R A C T

Spatially and timely accurate information about tropical forest disturbances is crucial for tracking critical forest changes, supporting forest management, and enabling law enforcement activities. In recent years, forest disturbance monitoring and alerting using cloud-penetrating Synthetic Aperture Radar (SAR) imagery has proven effective at national and pan-tropical scales. Related detection approaches mostly rely on detecting post-disturbance altered backscatter values in C or L-band SAR backscatter time series. Some disturbances are characterized by post-disturbance tree remnants or debris. For the time periods where these kinds of remnants remain present at the surface, the SAR backscatter values can be similar to those of stable forest. This can cause omission errors and delayed detection and it is considered a key shortcoming of current backscatter-based approaches. We hypothesized that despite fairly stable backscatter values, different orientation and arrangement of tree remnants leads to an altered heterogeneity of neighboring pixel values and that this can be quantified by textural features. We assessed six uncorrelated Gray-Level Co-Occurrence Matrix (GLCM) textural features using dense Sentinel-1C-band SAR time series. Forest disturbances, based on each GLCM feature using a pixel-based probabilistic change detection algorithm, were compared against results from forest disturbances mapped based only on backscatter data. We studied the impact of speckle-filtering on GLCM features and GLCM kernel sizes. We developed a method to combine backscatter and GLCM features, and we evaluated its robustness for a variety of natural and human-induced forest disturbance types across the Amazon Biome. Out of the six tested GLCM features GLCM Sum Average (SAVG) performed best. GLCM features derived from non-speckle filtered and speckle-filtered backscatter data did not show a noticeable impact on accuracy. A combination of backscatter and GLCM SAVG resulted in a reduced omission error of up to 36% and an improved timeliness of detections by average of to 30 days, with individual detection showing even higher improvements on a pixel level. The method was found to be robust across a variety of forest disturbance types. The largest reduction of omission errors and greatest improvement of timeliness was evident for sites with large unfragmented disturbance patches (e.g., large-scale clearings, fires and mining). For increasing GLCM kernel sizes, we observed a trade-off between reduced omission errors combined with improved timeliness and increasing commission errors. A kernel size of 5 was found to provide the best trade-off for reducing omission errors and improving timeliness while not introducing commission errors. The results emphasize that combining SAR-based textural features and backscatter can overcome omission errors caused by post-disturbance tree remnants or debris. This can help to improve the consistency and timelines of short (C-band) and long wavelength (L-band) based operational SAR disturbance monitoring and alerting. Result maps can be visualized via: https://johannesballing.users.earthengine.app/view/forest-disturbance-texture.

1. Introduction

Tropical forests are a key component of global biodiversity and the global carbon cycle (Boulton et al., 2022; Sullivan et al., 2017). Both human-induced and natural forest disturbances have increased in recent years and have been significantly harming tropical forests (Sande et al., 2019; Song et al., 2018). The ecological impact of forest disturbances varies considerably based on their type, intensity and the land

management practices at place (Bowd et al., 2021; Zambrano et al., 2020). Forest disturbances caused by human-induced land management practices include large-scale commercial logging, mining, smallholder agriculture, and selective logging (Curtis et al., 2018; Tyukavina et al., 2018), with many of these being unsustainable and illegal (Zimmerman and Kormos, 2012). Wildfire, windthrow, landslides, and meandering rivers are considered the dominant natural disturbances in the humid tropics (Espírito-Santo et al., 2014). Spatially and timely accurate information about new forest disturbances is crucial to empower policy makers and stakeholders to protect remaining forests and to reduce illegal and unsustainable activities (Moffette et al., 2021; Weisse et al., 2019).

Satellite-based remote sensing has proven a valuable tool for monitoring changes in humid tropical forests at large-scales (De Sy et al., 2012; Hirschmugl et al., 2020). Synthetic Aperture Radar (SAR) satellites are particularly capable in the tropics as radar signals are able to penetrate cloud cover (Ballère et al., 2021; Joshi et al., 2016). In the past, SAR-based forest disturbance monitoring relied mainly on long-wavelength L-band (~23 cm) radar from ALOS PALSAR and ALOS-2 PALSAR-2 (Achard and Hansen, 2016; Shimada et al., 2014). Since 2014, C-band data from Sentinel-1 satellites has been freely available, and a large number of studies have focused on exploiting the potential of dense short-wavelength radar for large-scale forest disturbance monitoring (Bullock et al., 2022; Langner and Carboni, 2021; Reiche et al., 2018a, 2018b; Ygorra et al., 2021). However, the deeper penetration depth and lower saturation level of L-band radar makes it more suitable for forest disturbance monitoring when compared to shorter wavelengths like C-band radar (~5.6 cm) (Ulaby and Long, 2013). While L-band radar penetrates through the top part of the forest canopy and interacts with larger tree elements including stems and branches, C-band radar mainly interacts with the smaller elements of the tree canopy including smaller branches and leaves in the top part of the canopy (Woodhouse, 2006).

In recent years, a number of SAR-based forest disturbance monitoring and alerting systems have been developed (e.g., RADD, JJ-FAST and Deter-B) (Doblas et al., 2022, Doblas et al. 2020; Hoekman et al., 2020; Reiche et al., 2021; Watanabe et al., 2021). These systems aim to detect new forest disturbances as quickly as possible with as few omission and commission errors as possible. Implemented detection methods analyze SAR backscatter time series and utilize altered post-disturbance backscatter values as an indicator of disturbed forest (Doblas et al., 2022; Reiche et al., 2021). For C-band disrupted or removed trees (e.g., branches, stems) lead to a reduction of direct surface scattering and/or a reduction of volume scattering resulting in decreased backscatter values in co– and cross-polarization respectively (Ulaby and Long, 2013; Woodhouse, 2006). For L-band similarly a reduction of volume scattering in the cross-polarization result in decreased backscatter values, whereas for co-polarization (especially HH) a gain of double-bounce at the tree trunks result in increased backscatter values (Watanabe et al 2021).

Some disturbance events, such as fires and logging, are characterized by post-disturbance tree remnants (e.g., disrupted trees, piles of tree remnants, low secondary vegetation) (Fig. 1).

Studies showed that tree remnants and debris can cause backscatter values similar to those of undisturbed forest (Balling et al., 2021; Hoekman et al., 2020) (Fig. 2). This might be the result of comparable or enhanced scatter mechanisms similar to those present for intact forest and can lead to a decrease in the forest/non-forest backscatter contrast. As a result, disturbances can go undetected, leading to omission errors or delayed detections in cases where the tree remnants are eventually removed (e.g., for preparing land for new cultivation). Large-scale forest disturbance events are predominantly affected, whereas for small-scale disturbances (e.g., logging roads, selective logging), a strong decrease in backscatter values is caused by radar shadow (Bouvet et al., 2018; Reiche et al., 2021). Stable radar backscatter from post-disturbance tree remnants is more dominant for shorter wavelengths, like X and C-band SAR data (Mitchell et al., 2014), but omission errors have also been observed for long wavelength L-band radar (Watanabe et al., 2021). These omission errors and delayed detections are evident in current SAR-based forest monitoring systems and are considered a major
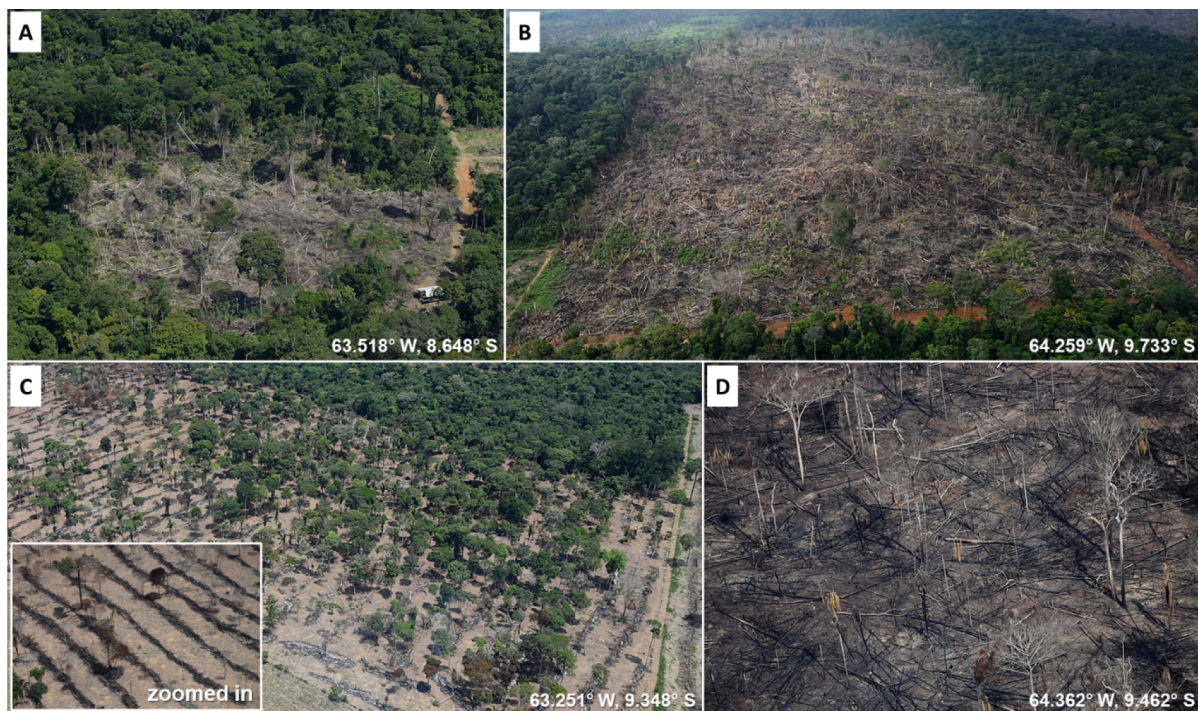

Fig. 1. Aerial photos of forest disturbances with post-disturbance tree remnants in the Brazilian Amazon. Medium (A) and large-scale (B) forest clearings, forest disturbance characterized by piled rows of tree remnants (C) and fire-related forest disturbance (D). Photos taken and provided by Juan Doblas/INPE/CEN-IMA-IBAMA.
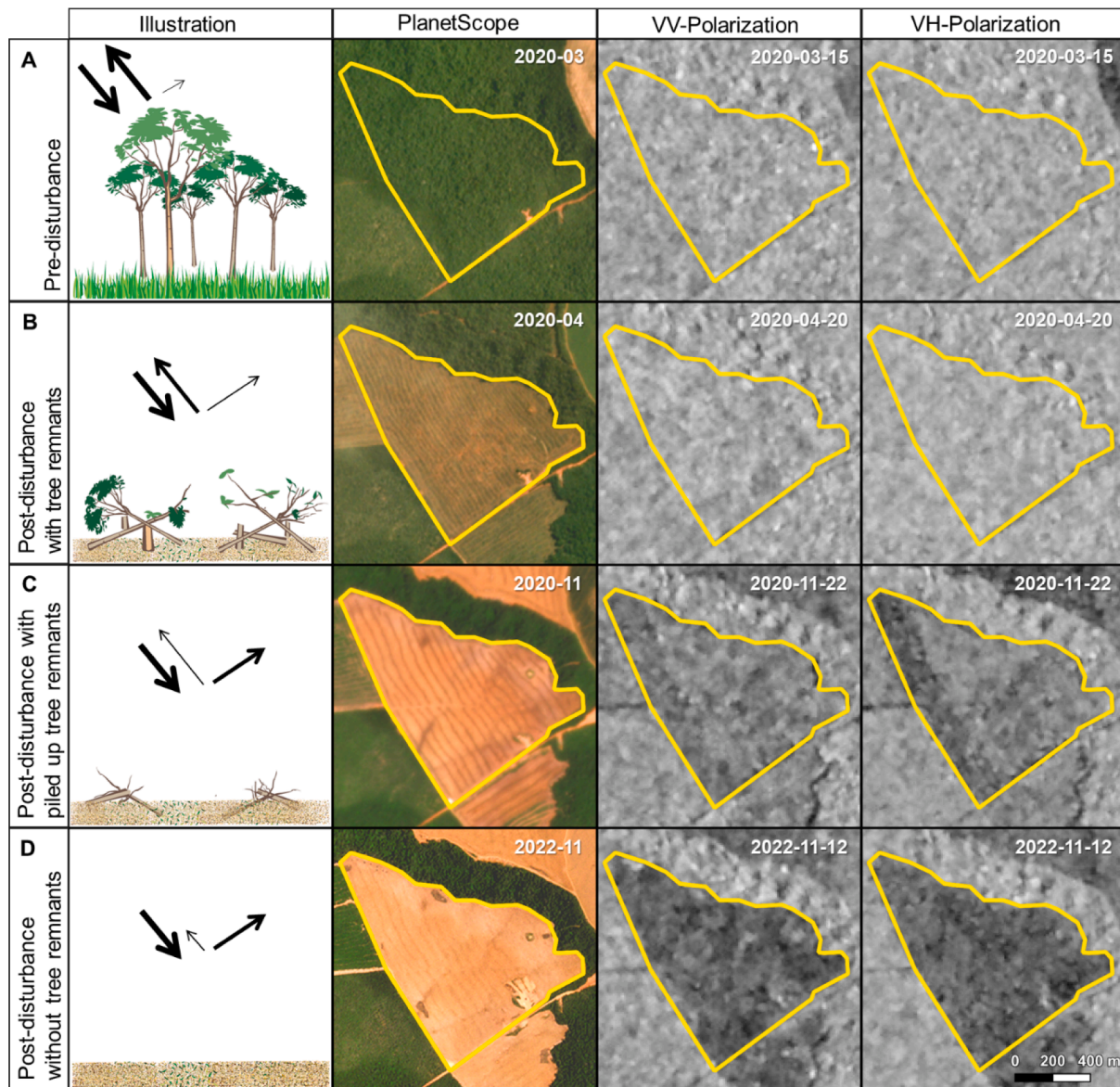
Fig. 2. Illustration of radar scattering in C-band wavelength (thickness of black arrows illustrates to the amount of energy) for a forest clearing associated with post-disturbance tree remnants. Stable forest (A) showing logging operations with tree remnants (B), which are piled up (C) and later removed (D). PlanetScope imagery (monthly composites) and Sentinel-1 backscatter images of VV- [min: −20 dB; max: 0 dB] and VH-polarization [min: −30 dB; max: −5 dB] are shown. Central coordinate: [59.676° W, 13.823° S].

shortcoming that has not yet been addressed (Doblas et al., 2022a). Delayed detections can be as vivid for monitoring and alerting systems as omission errors, as these decrease the timeliness of detections and hamper swift support of law enforcement tools.

Tree remnants and debris may alter the heterogeneity of the post-disturbance backscatter signal of adjacent pixels compared to the somewhat homogeneous pre-disturbance state of stable forest. This kind of heterogeneity of pixel values might be quantified by textural features. We hypothesize that textural features allow for a more complete and earlier detection of forest disturbances associated with tree remnants.

A variety of remote sensing studies have shown that including neighborhood information (adjacent pixels) by means of textural features can improve image analysis (Hamunyela et al., 2017, 2016; Jenicka and Suruliandi, 2014; Warner, 2011). Simple methods, such as including mean or standard deviation of adjacent pixel or high-/low-pass filters (e.g., Laplace or Sobel filter), do not account for the direct relationship with the neighboring pixel (Aquino et al., 2022; Warner, 2011). Textural features using the Gray-Level-Co-occurrence Matrix

(GLCM) (Haralick et al., 1973), however, take local adjacent neighboring pixels and their relationship into account (Hall-Beyer, 2017; Warner, 2011). A large variety of GLCM features have been developed since its introduction in the 1970 s and applied to SAR and optical-based land cover classification (Caballero et al., 2020; Chen et al., 2020; Kupidura, 2019), as well as to several forest applications (Abu et al., 2021; Champion et al., 2008; Danylo et al., 2021; Hethcoat et al., 2021; Niemi and Vauhkonen, 2016; Wood et al., 2012). Certain kernel sizes and pre-processing steps seem better suited for detecting and mapping different land cover types than others (Franklin et al., 2000; Tso and Mather, 1999). Studies showed the added benefit of GLCM features for detecting selective logging utilizing multi-sensor SAR data (Hethcoat et al., 2021). However, forest disturbance events besides selective logging (especially forest disturbance showing post-disturbance tree remnants) were not studied and the effect of pre-processing (speckle-filtering) and parameterization of the textural features (kernel sizes) was neglected. GLCM features might have the potential to quantify the changed heterogeneity associated with tree remnants and debris for

forest disturbances at large scales. However, the merit of GLCM features for improving the detection of humid tropical forest disturbances remains largely understudied.

This study assesses how GLCM features can improve forest disturbance mapping in the humid tropics using short-wavelength Sentinel-1C-band SAR data.

The objectives of this study are threefold:

- Evaluate different Sentinel-1-based GLCM features for forest disturbance mapping, and assess the effect of speckle-filtering and kernel size,
- Combine backscatter and GLCM features and evaluate its detection accuracy for a variety of forest disturbance types, and
- Assess the improvements in timeliness of forest disturbance detection

We used dense time series of Sentinel-1C-band backscatter data and six GLCM features to map forest disturbances at seven different sites across the Amazon Biome. Two sites (*development sites*) were used to develop a methodology to combine backscatter and GLCM textural features for forest disturbance mapping. Five additional sites (*testing sites*) were used to evaluate the robustness of the method for a variety of different natural and human-induced forest disturbance types by assessing detection accuracy and improvement of timeliness. We define timeliness as the date of which a disturbance is detected by the algorithm. Thus, improved timeliness is understood as an earlier detection date.

2. Study area and data

2.1. Study area

The study area consisted of seven humid tropical forest sites located within the Amazon Biome, each covering about 500 km^2 (Fig. 3). The Amazon Biome covers roughly 6.7 million km^2 and extends from the lowland coastline of Brazil in the East to mountainous areas of up to 6700 m elevation in Peru in the West (Davidson et al., 2012). Human-induced and natural forest disturbances have led to an estimated forest loss of up to 17% over the past 50 years (WWF, 2005). Human-induced forest disturbances are driven by medium to large-scale commodity agriculture, smallholder agriculture, mining and selective tree logging (Curtis et al., 2018). Fires and windthrows are considered the key natural disturbances in the Amazon Biome (Negrón-Juárez et al., 2018; Tyukavina et al., 2017).

Sites 1 and 2 were used as development sites to study the GLCM features and develop a method to combine backscatter and GLCM features for disturbance mapping (Table 1). Site 1 is located in the Amazonas State and is characterized by medium-scale forest clearings, whereas Site 2 experiences large-scale forest clearings and is located in the Mato Grosso State. These sites were selected as current alert systems (e.g., RADD) showed omission errors due to post-disturbance tree remnants when detecting forest disturbances using only backscatter time series (Reiche et al., 2021).

The additional sites 3–7 are located in Bolivia, Peru, and Suriname and were selected as prime examples to test the developed method for a range of different natural and human-induced forest disturbance types. These disturbance types include mining, selective logging, fires, windthrow, and small to medium-scale clearings in mountainous terrain.
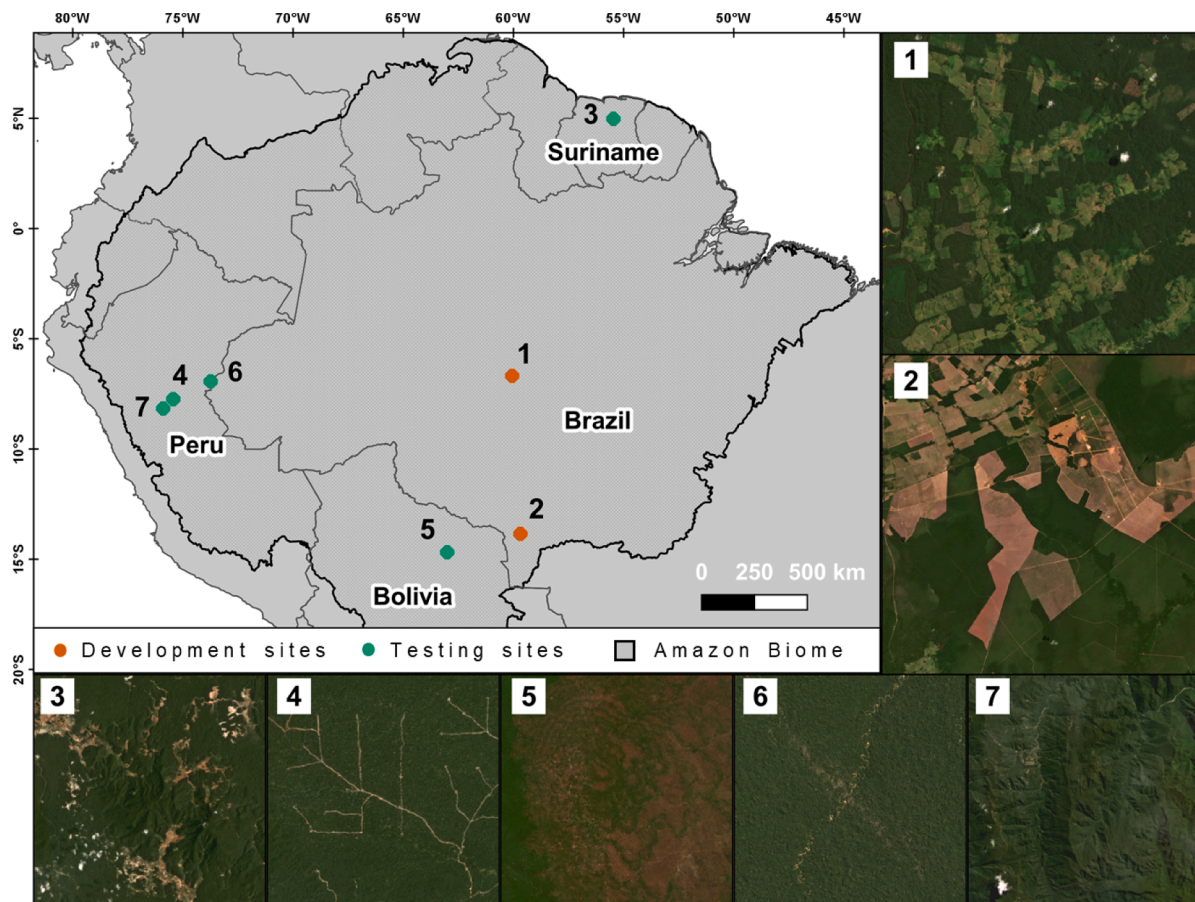

Fig. 3. Study area and locations of the two development and five testing sites. Monthly composites of PlanetScope imagery are shown for all study sites [note: 3–7 are zoomed-in images for improved visibility of the disturbance event].

Table 1
Site overview and description.

Site	Disturbance type	Description	Median disturbance patch size [ha]	Location [Central coordinates]
1	Medium-scale clearings	Medium-scale clearings associated partially with tree remnants located in fragmented forest	19.1	Brazil [60.068° W; 6.684° S]
2	Large-scale clearings	Large-scale clearings associated partially with tree remnants located in a mix of fragmented and intact forest	159.0	Brazil [59.689° W; 13.853° S]
3	Mining	Forest clearing associated to open-pit gold mining	0.7	Suriname [55.470° W; 4.975° N]
4	Selective logging	Network of logging roads accompanied by selective logging	0.3	Peru [75.445° W; 7.737° S]
5	Fire	Severe and large-scale forest fire with tree remnants (burned trees)	25.2	Bolivia [63.016° W; 14.687° S]
6	Windthrow	Tornado resulting in a string of small-scale forest disturbance patches	0.0.4	Peru [73.740° W; 6.940° S]
7	Mountainous terrain	Small to medium-scale forest disturbance patches in mountainous terrain	1.1	Peru [75.896° W; 8.165° S]

2.2. Sentinel-1 data

We used C-band Sentinel-1A/B radar data provided in Interferometric Wide swath dual-polarization (VV- and VH-polarization) mode. We accessed Sentinel-1 Ground Range Detected (GRD) data from 2018 to 2021 in Google Earth Engine, which was acquired in descending orbits with a temporal resolution of 12 days (ESA, 2022). Sentinel-1 GRD data has a spatial resolution of 20 m, with a pixel spacing of 10 m (ESA, 2012). Initial pre-processing was applied on the GRD data prior to ingestion in Google Earth Engine, including orbit positioning correction, GRD border noise removal, thermal noise removal, radiometric calibration, terrain correction and geocoding (Google Earth Engine Team, 2022). We also applied an angular-based radiometric slope correction, adaptive multi-temporal speckle filtering, and conversion from linear to dB scale (Mullissa et al., 2021; Quegan and Yu, 2001; Vollrath et al., 2020).

2.3. Forest baseline map and definitions

We generated a forest baseline map for our study period of 2020 (Reiche et al., 2021) using a Landsat-based primary humid tropical forest product of 2000 (Turubanova et al., 2018) and removed all pixels that indicated disturbances prior to the monitoring period (2001–2019) using an annual Landsat tree cover loss product (Hansen et al., 2013). We defined forest disturbances as *partial or complete removals of tree cover* within one Sentinel-1 pixel similar to other recent studies (Hansen et al., 2016, 2013; Reiche et al., 2021; Vargas et al., 2019).

3. Methods

3.1. GLCM features

Images can be understood as a grid of grey values, which can form local clusters of similar or dissimilar values (Warner, 2011). These local

clusters can be quantified by GLCM features (Armi and Fekri-Ershad, 2019). These GLCM features are calculated by first forming a matrix (a so-called 'grey level co-occurrence matrix'), in which the spatial relationship of adjacent pixel values to one another within a given *neighborhood* is expressed (Haralick et al., 1973). *Neighborhoods* are defined by a moving window or kernel around a central pixel (Hall-Beyer, 2017). GLCMs are formed for each central pixel's *neighborhood* throughout an entire image. A manifold of GLCM features have been developed (Conners et al., 1984) for detecting and describing certain similarities and dissimilarities (e.g., locating edges, expressing homogeneity) (Hall-Beyer, 2017). We selected six uncorrelated and meaningful GLCM features for testing our hypothesis (Table 2) and calculated them for different kernel sizes: 3, 5, 7, 9, 13, and 21 (Hall-Beyer, 2017; Haralick et al., 1973). Since the relationship of adjacent values within a GLCM depends on the look direction within the GLCM matrix, averages of four look directions (0°, 45°, 90°, and 135°) were calculated for each local GLCM separately (Warner, 2011). The six GLCM features were calculated for each Sentinel-1 image and VV and VH polarization separately. Studies showed the advantage of GLCM features derived from SAR data without speckle filtering over speckle-filtered SAR data in remote sensing applications (Chen et al., 2020; Marceau et al., 1990). We therefore calculated GLCM features based on Sentinel-1 data without speckle filtering and Sentinel-1 data with multi-temporal speckle filtering to assess the effect of speckle filtering.

3.2. Combining backscatter and GLCM features

We first mapped forest disturbances separately for each of the six GLCM features, kernel sizes and pre-processing scenarios (without speckle filtering and multi-temporal speckle filtering) and compared the results with forest disturbances that were mapped based only on backscatter information. These results were used to select the best performing GLCM feature and, subsequently, to combine backscatter and textural information for forest disturbance detection.

We used a pixel-based probabilistic change detection algorithm (Reiche et al., 2018a, 2015) to map forest disturbances and their respective disturbance dates for 2020 within the boundary of the forest baseline map. Time series of 2018 and 2019 were used as a historic period to calculate the mean and standard deviation of stable forest and to parametrize a Gaussian Mixture Model. The Gaussian Mixture Model was used to derive the non-forest probability of each new Sentinel-1 observation and afterwards used to detect and trigger a forest disturbance when a new observation diverted from the distribution of historical stable forest observations. Subsequent observations were used to increase confidence and confirm or reject the forest disturbances. The

Table 2
The six used GLCM features with p(i,j) being the probability of the (i,j)th entry in a GLCM matrix, and μ_x, μ_y, σ_x, σ_y are the means and standard deviations of p_x and p_y (Haralick et al., 1973).

GLCM textural measure	Abbreviation	Description	Equation
Angular Second Moment	ASM	Numbers of repeated pairs within a GLCM	$\sum_i\sum_j\{p(i,j)\}^2$
Correlation	COR	Correlation of pixel pairs within a GLCM	$\sum_i\sum_j\frac{(ij)p(i,j)-\mu_x\mu_y}{\sigma_x\sigma_y}$
Entropy	ENT	Randomness of grey-level distribution within a GLCM	$-\sum_i\sum_jp(i,j)\log(p(i,j))$
Inverse Difference Moment	IDM	Homogeneity of pixel pairs along the diagonal of a GLCM	$\sum_i\sum_j\frac{1}{1+(i-j)^2}p(i,j)$
Sum Average	SAVG	Average of pixel pairs within a GLCM	$\sum_{i=2}^{2N_g}ip_{x+y}(i)$
Variance	VAR	Variance of pixel pairs within a GLCM	$\sum_i\sum_j(i-\mu)^2p(i,j)$

date of the forest disturbance was set to the date of the image that first triggered the forest disturbance (Reiche et al., 2018a, 2015). The method was used to map forest disturbances for backscatter and all GLCM features separately. Hereby, co-polarization (VV) and cross-polarization (VH) were used to account for a change of the radar signal resulting from altered surface scattering/double bounce or volume scattering respectively. We applied a minimum mapping unit of 0.1 ha (8-connected Sentinel-1 pixels). More detailed information on the method and parametrization is given in Reiche et al. (2021).

After using the pixel-based probabilistic change detection algorithm to separately map disturbances using backscatter time series and the best performing GLCM feature time series we combined both detections.. Prior to combining, we applied an inverse buffer (shrinking detections) to the forest disturbances mapped using the GLCM feature to mask out blurring effects at forest edges resulting from the GLCM smoothing values of adjacent pixels (Fig. 4). As this blurring effect is directly linked to the kernel size, we defined the size of the inverse buffer as half of the kernel size. For disturbances present in both maps we selected the earliest detection date.

3.3. Validation and assessment of timeliness

High resolution multi-spectral PlanetScope data (~4.7 m) was used to visually check for the presence of forest disturbances and therefore to validate the mapped forest disturbances (Planet Team, 2022). In case of persistent cloud coverage hampering the visual interpretation of PlanetScope data, we used Sentinel-2, Landsat-7/-8 images or Sentinel-1 time series (ESA, 2015; USGS, 2019a, 2019b). We used a stratified random sampling approach with four strata: two stable forest strata and two forest disturbance strata (Olofsson et al., 2014). The two stable forest strata consisted of *stable forest – outside 200 m buffer* and *stable forest – inside a 200 m buffer* around detected forest disturbances. The latter was included to mitigate the effect of underrepresenting omission errors (Olofsson et al., 2020). The two forest disturbance classes were defined as *forest disturbance disagreement* – mapped in either the backscatter or GLCM feature and *forest disturbance agreement* – mapped in both backscatter and GLCM feature. Hereby, the strata forest disturbance disagreement was used to specifically reduce the effect of underrepresenting commission or omission errors in either the backscatter or GLCM feature forest disturbance detection. We used 500 samples for the development sites 1 and 2 and 250 samples for the testing sites 3–8. The samples were distributed equally between the stable forest classes (150: sites 1 and 2; 75: sites 3–8) and the disturbance classes (100: sites 1 and 2; 50: sites 3–8). The sample strata and area-statistics were created based on a combination map utilizing speckle filtered backscatter and GLCM SAVG derived from speckle filtered

backscatter (kernel size 9). As the samples of our sample design were not proportionally allocated to the strata areas we used sample inclusion probabilities (Stehman et al., 2003). Sample inclusion probabilities were calculated using strata areas and number of sample points. Estimation weights, i.e. the inverse of inclusion probability, were used to calculate User's Accuracy (UA) and Producer's Accuracy (PA) based on an area weighted confusion matrix (Stehman, 2014; Stehman et al., 2003). UA ($1 -$ comission error) and PA ($1 -$ omission error) were further used to calculate commission and omission errors respectively. Errors due to the underlying forest baseline map were noted in the response design, but they were excluded for calculating UA or PA. These errors were caused by omitted disturbances of 2019 due to cloud coverage in the optical remote sensing products, which was used to generate the forest baseline map (Verhelst et al., 2021).

We assessed the improvement of timeliness by comparing disturbances detected using backscatter time series and disturbances detected by combined backscatter and GLCM SAVG time series. We calculated the mean of the difference of forest disturbance dates. We only considered forest disturbances that were detected in backscatter and the combined backscatter and GLCM SAVG time series.

4. Results

4.1. GLCM features

Forest disturbances mapped using only backscatter information showed similar results for sites 1 and 2 (Fig. 5). The UA and corresponding standard errors for mapped disturbance using speckle filtered backscatter (Site 1: 95.1 ± 5.3% and Site 2: 98.2 ± 3.4%) were comparable to results achieved for non– backscatter without speckle filtering (Site 1: 98.6 ± 4.6% and Site 2: 100 ± 0%). The PA was higher for speckle filtered backscatter (Site 1: 64.0 ± 12.7% and Site 2: 81.9 ± 11.5%) compared to backscatter without speckle filtering (Site 1: 41.3 ± 12.1% and Site 2: 62.1 ± 14.1%). The low PA indicates omission errors related to the described post-disturbance tree remnants.

Forest disturbance mapped utilizing the six GLCM features showed similar results for sites 1 and 2. GLCM COR produced the poorest results with low PA regardless of pre-processing or varying kernel-size. The other GLCM features showed better results. Larger kernel sizes led to higher PA. However, most of the GLCM features showed low UA. For increasing kernel sizes, we observed a trade-off between increasing UA and decreasing PA (introducing commission errors). GLCM features calculated based on backscatter data without speckle filtering and backscatter data with multi-temporal speckle filtering resulted in similar accuracies. GLCM SAVG resulted in the best accuracy and showed higher PAs and UAs compared to the other GLCM features. The optimal kernel
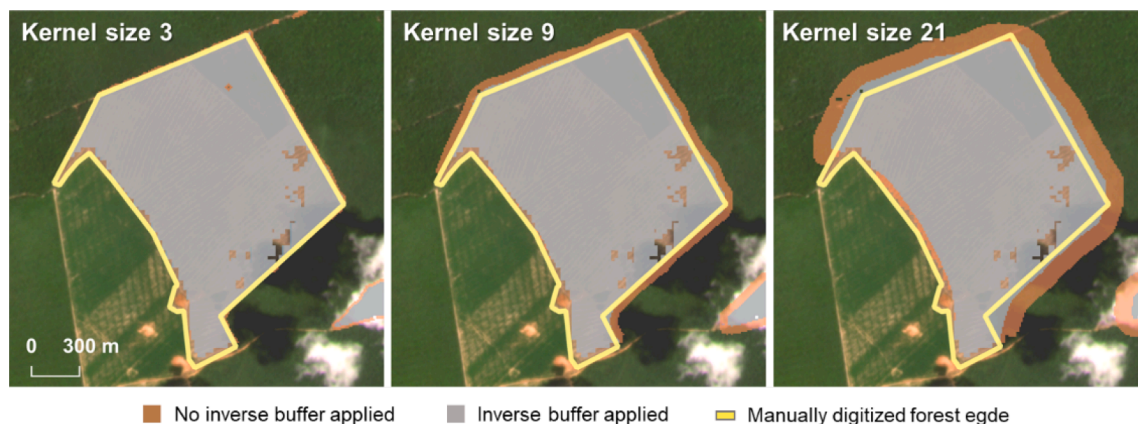
Fig. 4. Blurring effect of a GLCM feature along edges of forest clearings. Displayed are forest disturbances mapped utilizing GLCM SAVG based on kernel sizes 3, 9 and 21 without applied inverse buffer (orange) and with applied inverse buffer (grey). Additionally a manually digitized forest edge (yellow) is provided. A monthly composite of PlanetScope imagery for January 2021 is shown as a base map. [Central coordinate: 59.711° W, 13.822° S]
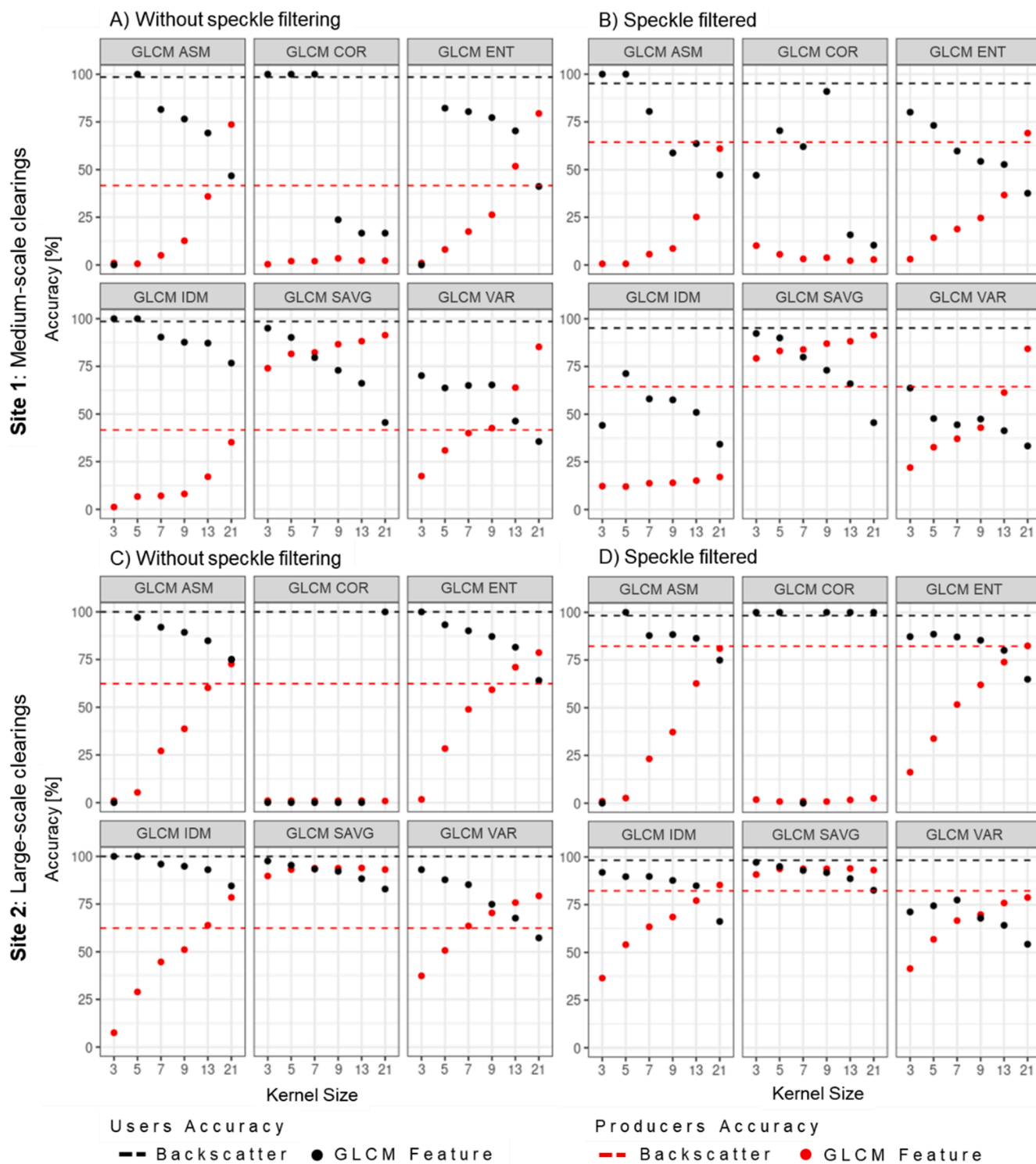
Fig. 5. UA (black) and PA (red) of mapped forest disturbances based on GLCM features for sites 1 and 2. GLCM features were calculated based on Sentinel-1 time series without speckle filtering (A and C) and Sentinel-1 time series with multi-temporal speckle filtering (B and D). UA and PA of backscatter time series are provided within the respective scatterplots as horizontal dashed lines. A description of the GLCM features are given in Table 2. See Appendix 1 for all accuracies ± standard errors.

size for GLCM SAVG – which can be understood as improved PA without reduced UA compared to the mapped disturbance based on backscatter alone – varied from 5 (Site 1) to 7 (Site 2) depending on the test site.

4.2. Combing backscatter and GLCM features

We used speckle filtered backscatter for the combination of

backscatter and GLCM SAVG features as they resulted in better initial PA when compared to backscatter without speckle filtering (Fig. 5). Out of the six tested GLCM features, GLCM SAVG showed the highest reduction of omission error, while introducing the lowest amount of new commission error for sites 1 and 2. We did not observe a difference in accuracies between disturbances mapped based on GLCM SAVG data derived from backscatter data without or with speckle filtering. The

remaining results are therefore presented based on speckle filtered backscatter and GLCM SAVG based on speckle filtered backscatter data.

The improvement from the combination of backscatter and GLCM SAVG was especially visible for larger patches, for which disturbances regularly were not detected in backscatter data alone (Fig. 6). Blurring effects at the edges of forests and disturbance patches present in the mapped disturbances using GLCM SAVG were not visible in the combination maps.

Results obtained based on combined backscatter and GLCM SAVG data showed similar UAs as disturbance mapped based on backscatter alone across all sites. The PA was found to improve for the combination of backscatter and GLCM SAVG. This was especially visible for sites showing medium-scale clearings, large-scale clearings, mining, and fires, for which we observed an increasing PA for increasing kernel sizes (Fig. 7). However, large kernel sizes of 7 and increasing resulted in lower UAs than the initial backscatter detection. Overall, the critical kernel size for an accuracy trade-off was 5 across all sites, with only *Large-scale clearings* showing kernel size 7 or even higher being optimal. For kernel sizes of 5, we found improved PA with less omission errors between 8 and 36%, while maintaining the UA of the initial backscatter results. For selective logging and windthrow, the combination of backscatter and GLCM SAVG did not show increased or decreased PA and UA.

4.3. Assessment of timeliness

Forest disturbances mapped by both backscatter information and by combined backscatter and GLCM SAVG information showed an improved timeliness of the detection based on combined information compared to backscatter data alone Areas with larger disturbance patches and areas with distinct tree remnants showed particular improvement in terms of timeliness (Fig. 8).

The largest temporal improvement was obtained for large-scale clearings (Site 2) and mining (Site 3), with disturbances being detected up to 34 days earlier on average (Table 3). Large standard deviations (up to 55 days) indicate even greater temporal improvements for individual disturbances. Results for medium-scale clearings (Site 1), fire (Site 5) and mountainous areas (Site 7) were smaller, with temporal improvements of up to 17 days on average. For these sites, we also observed earlier detections for larger kernel sizes compared to smaller kernel sizes. Negligible temporal improvements were visible for sites defined by windthrow and selective logging (<1.4 days).

5. Discussion

We showed how texture can be used to successfully overcome omission errors caused by post-disturbance tree remnants and eventually improve the quality of current monitoring and alerting systems. Post-disturbance tree remnants cause altered heterogeneity of neighboring backscatter pixels due to different composition and orientation. GLCM SAVG was the most effective in detecting the described heterogeneity. Our findings confirm the usefulness of GLCM SAVG for forest applications found by previous studies, which showed its benefit for mapping oil palm (Danylo et al., 2021), linking vegetation structure or biomass to remote sensing data (Niemi and Vauhkonen, 2016; Wood et al., 2012), and detecting selective logging (Hethcoat et al., 2021).

Our developed method strongly benefited from the combined use of backscatter and GLCM SAVG. GLCM SAVG texture improved detections of medium to large-scale events. Small-scale events such as selective logging were excluded in the GLCM SAVG disturbance mapping due to masking of blurring effects along disturbance patch edges. Backscatter allowed identifying such small-scale events due to its sensitivity to detect radar shadows (Bouvet et al., 2018). Combining backscatter and GLCM SAVG resulted in decreased omission errors of up to 36% when compared to disturbance detection based on backscatter alone.

Fig. 6. Forest disturbance dates [DoY] for combinations of backscatter and GLCM SAVG (kernel size 7) data for Site 1 (A) and Site 2 (B). Detailed maps are given for disturbances mapped based on backscatter (bottom left), GLCM SAVG (bottom middle) and a combination of both (bottom right). Combin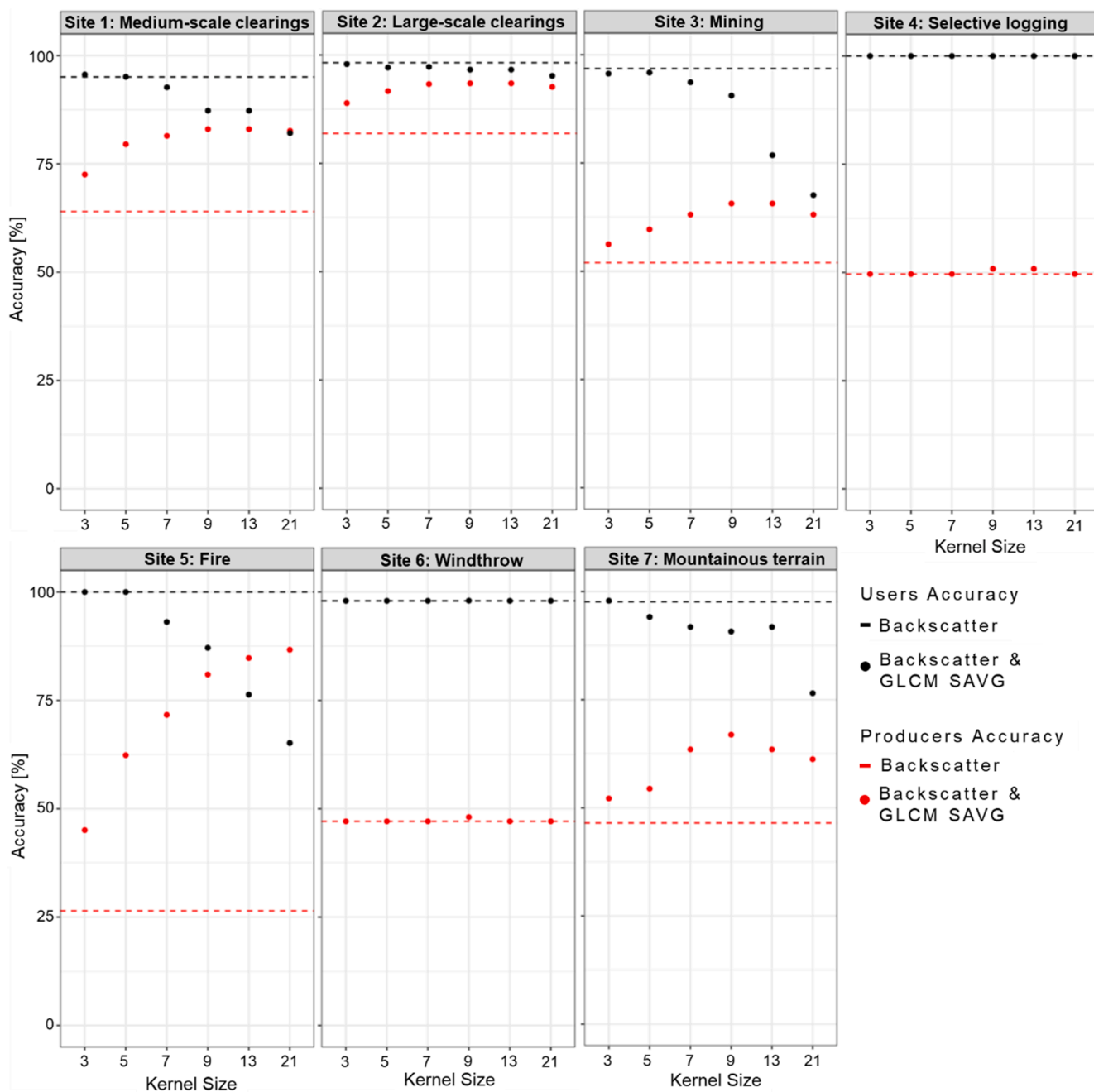ation results for all sites can be visualized via https://johannesballing.users.earthengine.app/view/forest-disturbance-texture.

Fig. 7. UA and PA for forest disturbances mapped for all test sites utilizing combined information of backscatter and GLCM SAVG data. UA and PA of mapped disturbances using only on backscatter information are also shown (dashed line). See Appendix 2 for all accuracies ± standard errors.

A kernel sizes of 5 was found best for reducing omission errors while not introducing new commission errors across all sites. Increased commission errors when using large kernel sizes were caused by spatial blurring along borders of disturbance patches and forest edges in the GLCM SAVG data (Zhang and Moore, 2015). To counteract these blurring effects, we implemented additional edge masking using an inverse buffer. Outer edges of disturbances detected based on GLCM SAVG were masked based on a GLCM kernel-size dependent buffer. Despite this masking, we observed increased commission errors for larger kernel sizes (>=7) for some test sites. Larger kernel sizes led to merging of multiple neighboring small disturbance patches into a single disturbance patch. This did not allow to exclude blurred edge areas of the small patches via the proposed edge masking. This was evident for test sites characterized by medium-sized disturbance patches and fragmented forest (e.g., medium-scale logging, mining) (Fig. 7).

We observed a general steady decrease of omission errors with increasing kernel-sizes due to an inclusion of more adjacent pixels and therefore a higher chance of detecting changed heterogeneity. However, for some disturbance types (medium-scale clearings, mining, and mountainous terrain), larger kernel sizes (>=13) resulted in fewer increased omission errors (Fig. 7). This can be linked to the proposed masking of the GLCM SAVG disturbance map, which excludes smaller isolated disturbance patches via the kernel-size dependent inverse buffer. Hereby, larger kernel sizes result in same size disturbance patches as smaller kernel sizes but, at the same time, an increased buffer excludes valid disturbance detection. This might explain why disturbance types characterized by smaller disturbance patches (e.g., windthrow, selective logging) did not show increased accuracies when using GLCM SAVG as shown in other studies (Hethcoat et al., 2021). Follow-up studies might explore the possibility of including the size of a
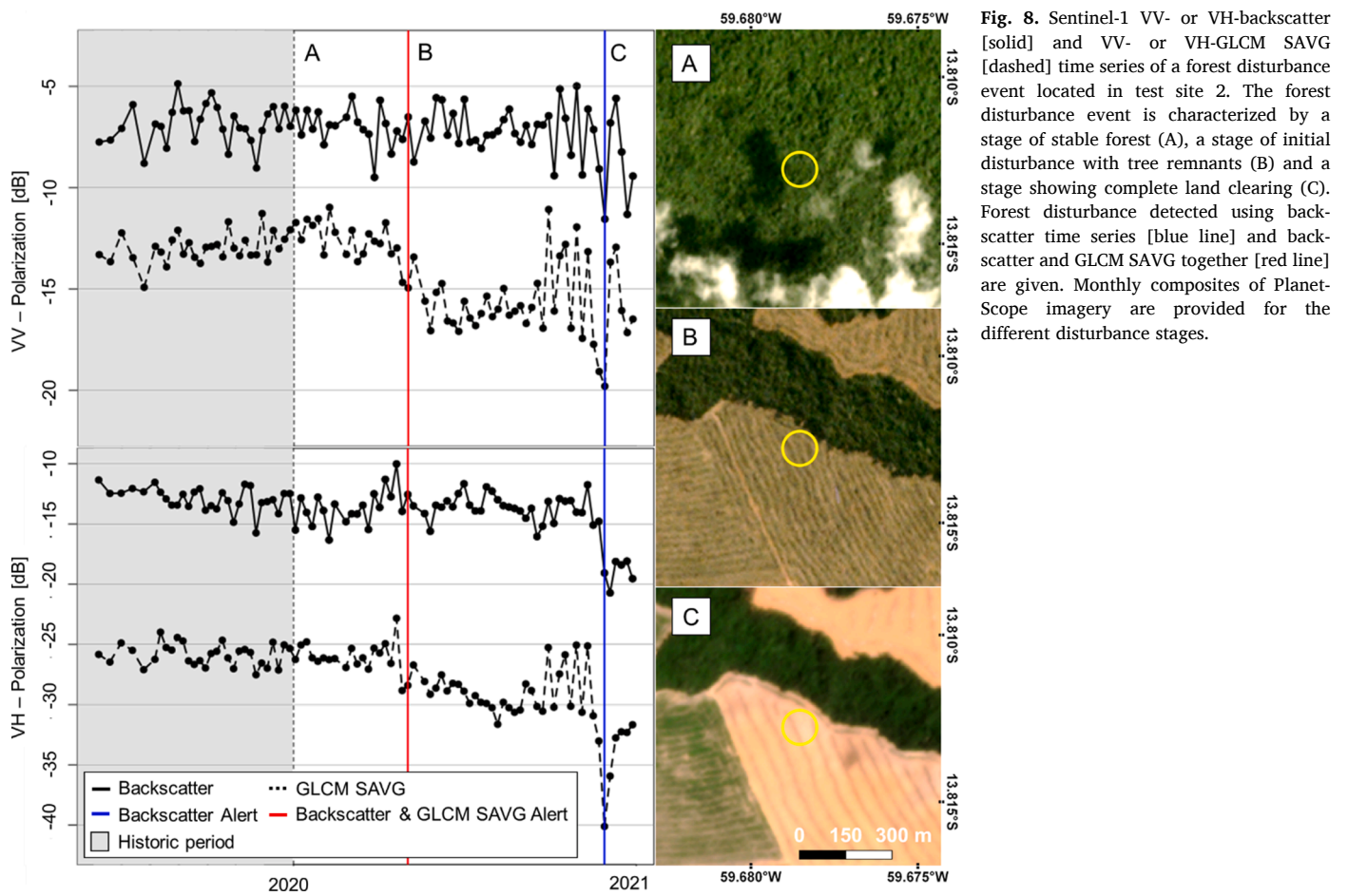
Fig. 8. Sentinel-1 VV- or VH-backscatter [solid] and VV- or VH-GLCM SAVG [dashed] time series of a forest disturbance event located in test site 2. The forest disturbance event is characterized by a stage of stable forest (A), a stage of initial disturbance with tree remnants (B) and a stage showing complete land clearing (C). Forest disturbance detected using backscatter time series [blue line] and backscatter and GLCM SAVG together [red line] are given. Monthly composites of Planet-Scope imagery are provided for the different disturbance stages.

Table 3

Mean temporal improvement in days (bold) ± standard deviation of disturbances mapped using combined backscatter and GLCM SAVG data compared to backscatter data alone.

Site	Kernel Size					
	3	5	7	9	13	21
Site 1: Medium-scale clearings	9.5 ± 17.0	13.5 ± 20.6	16.0 ± 22.1	16.7 ± 22.3	16.9 ± 21.6	15.5 ± 19.9
Site 2: Large-scale clearings	22.2 ± 32.0	29.8 ± 36.0	32.7 ± 37.3	33.7 ± 37.8	34.3 ± 38.4	33.8 ± 38.8
Site 3: Mining	14.3 ± 37.1	19.8 ± 45.2	22.8 ± 49.8	23.8 ± 52.2	24.3 ± 54.5	22.3 ± 54.5
Site 4: Selective logging	0.9 ± 6.5	0.8 ± 6.4	0.4 ± 4.6	0.3 ± 3.5	0.1 ± 2.5	0.0 ± 1.6
Site 5: Fire	7.8 ± 10.3	10.4 ± 11.6	11.8 ± 12.1	12.5 ± 12.4	12.9 ± 12.4	12.7 ± 11.9
Site 6: Windthrow	1.4 ± 12.4	0.8 ± 9.6	0.2 ± 4.6	0.0 ± 2.5	0.0 ± 0	0.0 ± 0
Site 7: Mountainous terrain	9.1 ± 27.8	10.5 ± 31.3	10.8 ± 32.4	9.7 ± 31.2	8.3 ± 29.0	5.5 ± 23.3

disturbance patch and its fragmentation in addition to the kernel size in the masking of disturbances mapped using GLCM SAVG.

Combining backscatter and GLCM SAVG data resulted in more timely disturbance detections when compared to disturbances detected by backscatter alone. Larger kernel sizes led to increased improvement in timeliness. However, increasing kernel sizes also led to increased commission error. This trade-off needs to be considered when assessing optimal kernel sizes. Spatially optimal GLCM SAVG kernel sizes of 5 improved the timeliness of detections between 10 and 30 days on average. Individual disturbance events repeatedly showed an improved timeliness of 2 to 3 months. It is important to stress that for many applications timeliness of detections can be of equal importance as spatial accuracy (Bullock et al., 2022, Reiche et al. 2018a). Timely information is crucial to support effective law enforcement tools, especially for near real-time alerting systems.

No differences in accuracies for the previously applied speckle filtering of the backscatter data used to calculate GLCM SAVG were observed. Other studies showed that GLCM SAVG based on SAR data without speckle filtering resulted in superior accuracy for land cover classifications (Chen et al., 2020). The insignificance of speckle-filtering in our study may be explained by the use of multi-look Sentinel-1 GRD data, and results may vary when using single-look complex data.

Assessing performance individually for several sites allowed us to show the benefit of textural features for specific forest disturbance types. This showed a wide range of spatial and temporal improvements. Using one larger region only would have led to averaged accuracies and would have not allowed to study the advantages and disadvantages on combining backscatter and GLCM SAVG in such detail.

It is expected that SAR-based monitoring systems operating at longer wavelength (e.g., L-band) will also benefit from using GLCM SAVG for overcoming reported omission errors due to post-disturbance tree remnants (Watanabe et al., 2021). Different orientations and composition of tree remnants and debris are expected to alter the heterogeneity of neighboring pixel values at L-band similar to C-band.

6. Conclusion

We have showed that textural features can overcome omission errors in SAR-based forest disturbance detections caused by post-disturbance tree remnants. We tested six GLCM textural features derived from C-band Sentinel-1 time series. GLCM SAVG performed best. We developed a method that combines backscatter and GLCM SAVG. The proposed method has proven robust across a variety of forest disturbance types in the Amazon Biome. Forest disturbance detections showed reduced omission errors of up to 36% and improved timelines of up to on average 30 days when compared against backscatter detections. We observed a trade-off for larger GLCM kernel sizes leading to higher improvements of timeliness and a reduction of omission error, while introducing increasing commission error. GLCM kernel size of 5 proved to be optimal, as it consistently led to spatial and temporal improvements, without introducing new commission error. Our method showed the largest spatial and temporal improvement for disturbance types characterized by large unfragmented disturbance patches (e.g., large-scale clearings, mining and fires). Large-area SAR-based monitoring and alerting systems can strongly benefit from the proposed method to further improve their consistency and robustness. Increasing accuracy and timeliness of forest disturbance mapping in the tropics is crucial to law enforcement and forest management activities to reduce illegal and unsustainable forest practices.

CRediT authorship contribution statement

Johannes Balling: Conceptualization, Methodology, Software, Validation, Formal analysis, Investigation, Writing – original draft, Writing – review & editing, Visualization. **Martin Herold:** Conceptualization, Writing – review & editing, Supervision, Project administration, Funding acquisition. **Johannes Reiche:** Conceptualization, Methodology, Writing – review & editing, Supervision, Project administration, Funding acquisition.

Declaration of Competing Interest

The authors declare that they have no known competing financial interests or personal relationships that could have appeared to influence the work reported in this paper.

Data availability

Data will be made available on request.

Acknowledgments

Appendix A:

Appendix 1

UA, PA and corresponding standard error [%] of mapped forest disturbances using backscatter or GLCM features derived from backscatter data with and without speckle-filtering for sites 1 and 2. Results of disturbances detected by a GLCM features are given for different GLCM kernel sizes (Ks).

	UA ± standard error						PA ± standard error					
Site 1: Without speckle filtering												
Back-scatter	98.6 ± 4.6						41.3 ± 12.1					
Kernel size	Ks 3	Ks 5	Ks7	Ks 9	Ks 13	Ks 21	Ks3	Ks 5	Ks7	Ks 9	Ks 13	Ks 21
GLCM ASM	0 ± 0	100 ± 0	81.1 ±31.6	76.3 ±22.5	69 ±21.0	46.6 ±20.9	0 ±0	0.6 ±1.9	5.0 ±5.3	12.6 ±8.1	35.9 ±12.8	73.6 ±14.0
GLCM COR	100 ± 0	100 ±0	100 ±0	23.4 ±72.5	16.5 ±57.1	16.5 ±57.1	0.4 ±1.2	2 ±3.2	2 ±3.2	3.4 ±4.4	2.2 ±3.5	2.2 ±3.5
GLCM ENT	0 ±0	82 ±26.7	80.1 ±18.2	77.0 ±19.7	70.1 ±18.2	41.1 ±18.0	0 ±0	8 ±6.6	17.4 ±9.3	26.2 ±11.7	51.7 ±14.1	79.4 ±13.8
GLCM IDM	100 ±0	100 ±0	90.1 ±21.1	87.3 ±21.6	87.0 ±15.9	76.5 ±20.1	1.2 ±2.7	6.7 ±6.1	7.1 ±6.3	8.0 ±6.6	17.0 ±9.2	35.1 ±12.2
GLCM SAVG	94.9 ± 5.2	90 ±8.3	79.5 ±14.0	72.9 ±14.5	66.1 ±14.3	45.5 ±16.8	73.9 ±14.4	81.5 ±14.6	82.3 ±14.6	86.6 ±13.5	88.2 ±12.7	91.3 ±10.5
GLCM VAR	69.9 ±30.1	63.6 ±24.7	64.9 ±21.8	65.1 ±20.1	46.2 ±23.6	35.5 ±14.9	17.4 ±10.3	30.9 ±13.2	39.9 ±13.7	42.6 ±13.4	63.8 ±14.0	85.3 ±10.7
Site 1: With speckle filtering												
Back-scatter	95.1 ± 5.3						64 ± 12.7					
Kernel size	Ks 3	Ks 5	Ks7	Ks 9	Ks 13	Ks 21	Ks3	Ks 5	Ks7	Ks 9	Ks 13	Ks 21
GLCM ASM	100 ±0	100 ±0	80.3 ±33.5	58.5 ±41.5	63.4 ±24.1	47.2 ±20.5	0.6 ±1.9	0.6 ±1.9	5.6 ±5.6	8.6 ±6.7	25.1 ±11.5	61.0 ±14.3
GLCM COR	46.8 ±93.8	70.3 ±59.6	61.9 ±80.5	90.7 ±28.1	15.6 ±51.6	10.2 ±26.0	10.2 ±7.1	5.6 ±5.4	3.2 ±4.2	3.8 ±4.6	2.2 ±3.5	2.8 ±4.0
GLCM ENT	79.6 ±42.1	72.9 ±30.5	59.5 ±30.2	54.1 ±24.4	52.6 ±20.3	37.5 ±17.7	3.0 ±4.2	14.2 ±9.7	18.8 ±10.5	24.6 ±11.5	36.7 ±13.2	69.1 ±13.9
GLCM IDM	43.8 ±70.8	71.0 ±34.2	57.9 ±35.6	57.3 ±34.7	50.7 ±29.8	34.1 ±34.7	12.2 ±9.3	12.0 ±9.2	13.8 ±9.5	14.0 ±9.6	15.2 ±9.8	17.1 ±10.1
GLCM SAVG	92.2 ±8.4	89.8 ±8.2	79.8 ±13.9	72.9 ±14.5	65.9 ±14.3	45.5 ±16.8	79.2 ±14.4	83.1 ±14.1	83.8 ±14.1	87.0 ±13.5	88.2 ±12.7	91.3 ±10.5
GLCM VAR	63.5 ±29.5	47.6 ±35.0	44.3 ±28.2	47.3 ±27.2	41.2 ±20.3	33.3 ±13.5	22.0 ±11.8	32.7 ±13.3	37.1 ±13.6	42.9 ±13.7	61.4 ±14.1	84.3 ±10.9
Site 2: Without speckle filtering												

Appendix 1 (*continued*)

	UA ± standard error						PA ± standard error					
Site 1: Without speckle filtering												
Back-scatter	98.6 ± 4.6						41.3 ± 12.1					
Kernel size	Ks 3	Ks 5	Ks7	Ks 9	Ks 13	Ks 21	Ks3	Ks 5	Ks7	Ks 9	Ks 13	Ks 21
Back-scatter	100 ± 0						62.1 ± 14.1					
Kernel size	Ks 3	Ks 5	Ks7	Ks 9	Ks 13	Ks 21	Ks3	Ks 5	Ks7	Ks 9	Ks 13	Ks 21
GLCM ASM	0	97	91.8	89.0	84.5	74.8	0	5.3	27.0	38.6	60.0	72.6
	±0	±9.6	±11.3	±10.9	±9.5	±8.4	±0	±6.4	±12.8	±14.1	±14.5	±14.2
GLCM COR	0	0	0	0	0	100	0	0	0	0	0	0.8
	±0	±0	±0	±0	±0	±0	±0	±0	±0	±0	±0	±2.6
GLCM ENT	100	93.1	89.8	86.8	81.0	63.5	1.7	28.2	48.7	59.0	70.8	78.5
	±0	±10.7	±9.2	±9.2	±8.7	±13.1	±3.7	±13.0	±14.6	±14.6	±14.1	±14.0
GLCM IDM	100	100	95.9	94.7	92.8	84.2	7.5	28.8	44.5	50.9	63.7	78.3
	±0	±0	±7.0	±6.9	±7.0	±13.7	±7.6	±13.1	±14.4	±14.6	±14.3	±13.4
GLCM SAVG	97.6	95.3	93.2	92.0	88.0	82.5	89.6	93.1	93.7	93.7	93.9	93.1
	±3.6	±4.7	±5.5	±5.9	±6.7	±7.1	±12.5	±12.8	±12.8	±12.8	±12.8	±13.0
GLCM VAR	92.9	87.4	84.8	74.5	67.2	56.7	37.2	50.5	63.3	70.2	75.6	79.2
	±9.2	±9.9	±9.5	±19.5	±17.2	±14.5	±14.0	±14.7	±13.3	±12.0	±11.2	±10.8
Site 2: With speckle filtering												
Back-scatter	98.2 ± 3.4						81.9 ± 11.5					
Kernel size	Ks 3	Ks 5	Ks7	Ks 9	Ks 13	Ks 21	Ks3	Ks 5	Ks7	Ks 9	Ks 13	Ks 21
GLCM ASM	0	100	87.6	88.1	86.0	74.4	0	2.7	23.1	37.1	62.5	80.9
	±0	±0	±14.9	±11.7	±9.1	±11.5	±0	±4.6	±12.2	±14.0	±14.4	±13.6
GLCM COR	100	100	0	100	100	100	1.8	0.8	0	0.8	1.7	2.5
	±0	±0	±0	±0	±0	±0	±3.7	±2.6	±0	±2.6	±3.7	±4.5
GLCM ENT	87.0	88.3	86.8	85.0	79.6	64.3	16.1	33.7	51.5	61.8	73.8	82.3
	±17.7	±11.8	±9.9	±9.2	±8.5	±11.0	±10.6	±13.7	±14.7	±14.6	±14.0	±13.7
GLCM IDM	91.7	89.4	89.5	87.4	84.5	65.7	36.4	53.9	63.2	68.3	76.9	85.2
	±10.0	±8.9	±8.1	±8.3	±8.0	±15.6	±14.0	±14.7	±14.4	±14.1	±13.6	±13.2
GLCM SAVG	97.1	94.6	92.8	91.6	88.4	82.1	90.7	93.7	93.7	93.7	93.9	93.1
	±3.9	±4.9	±5.6	±6.0	±6.7	±7.1	±12.7	±12.8	±12.8	±12.8	±12.8	±13.0
GLCM VAR	70.9	74.1	77.1	67.5	63.7	53.8	41.4	56.7	66.5	69.6	75.8	78.7
	±28.9	±23.1	±18.5	±20.5	±15.8	±14.1	±14.3	±14.8	±12.9	±12.4	±11.4	±11.2

Appendix 2

UA, PA and corresponding standard error [%] for forest disturbances mapped for all test sites using backscatter data, GLCM SAVG or combined information of backscatter and GLCM SAVG data. Results for the combined forest disturbance method are shown for different GLCM kernel sizes (Ks).

	UA ± standard error												
	Backscatter	GLCM SAVG						Backscatter & GLCM SAVG					
		Ks 3	Ks 5	Ks7	Ks 9	Ks 13	Ks 21	Ks 3	Ks 5	Ks7	Ks 9	Ks 13	Ks 21
Site 1	95.1	100.0	99.0	96.2	89.2	89.2	82.7	95.6	95.1	92.7	87.3	87.3	82.1
	±5.3	±0	±2.2	±4.0	±6.3	±6.3	±13.0	±4.7	±4.7	±5.3	±6.3	±6.3	±11.5
Site 2	98.2	98.4	97.8	97.9	97.2	97.2	95.7	97.9	97.1	97.3	96.6	96.6	95.2
	±3.4	±3.6	±3.5	±3.1	±3.2	±3.2	±4.6	±3.6	±3.6	±3.2	±3.3	±3.3	±4.6
Site 3	96.8	98.1	98.2	95.1	90.7	73.3	58.0	95.6	95.9	93.7	90.6	76.8	67.6
	±4.9	±4.2	±4.0	±6.0	±7.6	±38.9	±43.1	±5.4	±5.1	±6.0	±6.8	±32.5	±36.5
Site 4	100.0	100.0	100.0	100.0	100.0	100.0	100.0	100.0	100.0	100.0	100.0	100.0	100.0
	±0	±0	±0	±0	±0	±0	±0	±0	±0	±0	±0	±0	±0
Site 5	100.0	100.0	100.0	93.1	87.1	76.3	65.0	100.0	100.0	93.1	87.1	76.3	65.2
	±0	±0	±0	±7.4	±8.8	±9.8	±8.8	±0	±0	±7.4	±8.8	±9.8	±8.7
Site 6	98.0	100.0	100.0	100.0	100.0	100.0	100.0	98.0	98.0	98.0	98.0	98.0	98.0
	±4.5	±0	±0	±0	±0	±0	±0	±4.5	±4.5	±4.5	±4.5	±4.5	±4.5
Site 7	97.6	100	91.8	89.2	87.5	88.4	63.6	97.9	94.1	91.8	90.8	91.8	76.5
	±5.2	±0	±11.9	±10.9	±11.1	±11.7	±59.4	±4.6	±7.2	±7.6	±7.8	±7.6	±43.3
	PA ± standard error												
Site 1	64.0	66.4	74.6	78.0	77.2	77.2	77.7	72.5	79.5	81.5	83.0	83.0	82.6
	±12.7	±13.6	±14.5	±14.8	±14.7	±14.7	±14.8	±14.1	±14.9	±15.1	±15.2	±15.2	±15.2
Site 2	81.9	86.6	91.0	92.6	92.3	92.3	91.0	88.9	91.7	93.3	93.5	93.5	92.6
	±11.5	±12.7	±12.7	±12.8	±12.8	±12.8	±12.9	±12.5	±12.7	±12.9	±12.9	±12.9	±12.8
Site 3	52.0	43.5	46.1	50.3	50.3	49.8	39.5	56.2	59.7	63.1	65.6	65.6	63.1
	±26.8	±22.6	±23.9	±26.0	±26.0	±26.0	±21.4	±28.9	±30.5	±32.1	±33.3	±33.3	±32.1
Site 4	49.6	8.8	5.4	3.0	3.2	2.0	0.1	49.6	49.6	49.6	50.8	50.8	49.6
	±46.7	±10.0	±6.5	±3.7	±3.9	±3.1	±0.1	±46.7	±46.7	±46.7	±47.7	±47.7	±46.7
Site 5	26.5	44.5	61.8	71.7	81.0	84.8	86.2	45.1	62.3	71.7	81.0	84.8	86.7
	±3.6	±10.5	±11.1	±10.8	±9.1	±8.8	±8.7	±10.4	±11.4	±10.8	±9.1	±8.8	±8.6
Site 6	47.1	1.1	2.1	0.1	1.1	0	0	47.1	47.1	47.1	48.1	47.1	47.1
	±47.1	±2.4	±3.7	±0.1	±2.5	±0	±0	±47.1	±47.1	±47.1	±48.0	±47.1	±47.1
Site 7	46.5	27.1	25.3	37.4	39.7	34.7	30.9	52.2	54.4	63.5	66.9	63.5	61.2
	±30.5	±18.8	±17.4	±25.0	±26.4	±23.5	±21.3	±33.8	±35.2	±40.4	±42.3	±40.4	±39.1

References

Abu, I.-O., Szantoi, Z., Brink, A., Robuchon, M., Thiel, M., 2021. Detecting cocoa plantations in Côte d'Ivoire and Ghana and their implications on protected areas. Ecol Indic 129, 107863. https://doi.org/10.1016/j.ecolind.2021.107863.

Achard, F., Hansen, M.C., 2016. Global forest monitoring from earth observation. CRC Press, Boca Raton.

Aquino, C., Mitchard, E.T.A., Mcnicol, I.M., Carstairs, H., Burt, A., Luz, B., Vilca, P., Mayta, S., Disney, M., 2022. Detecting tropical forest degradation using optical satellite data : An experiment in peru show texture At 3 M gives best results. Preprints (Basel) 1–21. https://doi.org/10.20944/preprints202202.0141.v1.

Armi, L., Fekri-Ershad, S., 2019. Texture image analysis and texture classification methods - A review CoRR, 2, 1–29. https://doi.org/10.48550/arXiv.1904.06554.

Ballère, M., Bouvet, A., Mermoz, S., Le Toan, T., Koleck, T., Bedeau, C., André, M., Forestier, E., Frison, P.-L., Lardeux, C., 2021. SAR data for tropical forest disturbance alerts in French Guiana: Benefit over optical imagery. Remote Sens Environ 252, 112159. https://doi.org/10.1016/j.rse.2020.112159.

Balling, J., Verbesselt, J., de Sy, V., Herold, M., Reiche, J., 2021. Exploring archetypes of tropical fire-related forest disturbances based on dense optical and radar satellite data and active fire alerts. Forests 12, 456. https://doi.org/10.3390/f12040456.

Boulton, C.A., Lenton, T.M., Boers, N., 2022. Pronounced loss of Amazon rainforest resilience since the early 2000s. Nat Clim Chang 12. https://doi.org/10.1038/s41558-022-01287-8.

Bouvet, A., Mermoz, S., Ballère, M., Koleck, T., le Toan, T., 2018. Use of the SAR shadowing effect for deforestation detection with sentinel-1 time series. Remote Sens (Basel) 10, 1250. https://doi.org/10.3390/rs10081250.

Bowd, E., Blanchard, W., McBurney, L., Lindenmayer, D., 2021. Direct and indirect disturbance impacts on forest biodiversity. Ecosphere 12. https://doi.org/10.1002/ecs2.3823.

Bullock, E.L., Healey, S.P., Yang, Z., Houborg, R., Gorelick, N., Tang, X., Andrianirina, C., 2022. Timeliness in forest change monitoring: A new assessment framework demonstrated using Sentinel-1 and a continuous change detection algorithm. Remote Sens Environ 276, 113043. https://doi.org/10.1016/j.rse.2022.113043.

Caballero, G.R., Platzeck, G., Pezzola, A., Casella, A., Winschel, C., Silva, S.S., Ludueña, E., Pasqualotto, N., Delegido, J., 2020. Assessment of multi-date sentinel-1 polarizations and GLCM texture features capacity for onion and sunflower classification in an irrigated valley: An object level approach. Agronomy 10, 845. https://doi.org/10.3390/agronomy10060845.

Champion, I., Dubois-Fernandez, P., Guyon, D., Cottrel, M., 2008. Radar image texture as a function of forest stand age. Int J Remote Sens 29, 1795–1800. https://doi.org/10.1080/01431160701730128.

Chen, S., Useya, J., Mugiyo, H., 2020. Decision-level fusion of Sentinel-1 SAR and Landsat 8 OLI texture features for crop discrimination and classification: case of Masvingo. Zimbabwe. Heliyon 6, e05358.

Conners, R.W., Trivedi, M.M., Harlow, C.A., 1984. Segmentation of a high-resolution urban scene using texture operators. Comput Vis Graph Image Process 25, 273–310. https://doi.org/10.1016/0734-189X(84)90197-X.

Curtis, P.G., Slay, C.M., Harris, N.L., Tyukavina, A., Hansen, M.C., 2018. Classifying drivers of global forest loss. Science 1979 (361), 1108–1111. https://doi.org/10.1126/science.aau3445.

Danylo, O., Pirker, J., Lemoine, G., Ceccherini, G., See, L., McCallum, I., Hadi, K.F., Achard, F., Fritz, S., 2021. A map of the extent and year of detection of oil palm plantations in Indonesia, Malaysia and Thailand. Sci Data 8, 1–9. https://doi.org/10.1038/s41597-021-00867-1.

Davidson, E.A., de Araújo, A.C., Artaxo, P., Balch, J.K., Brown, I.F., Bustamante, C., Coe, M.M., DeFries, M.T., Keller, R.S., Longo, M., Munger, J.W., Schroeder, W., Soares-Filho, B.S., Souza, C.M., Wofsy, S.C., 2012. The Amazon basin in transition. Nature 481, 321–328. https://doi.org/10.1038/nature10717.

De Sy, V., Herold, M., Achard, F., Asner, G.P., Held, A., Kellndorfer, J., Verbesselt, J., 2012. Synergies of multiple remote sensing data sources for REDD+ monitoring. Curr Opin Environ Sustain 4, 696–706. https://doi.org/10.1016/j.cosust.2012.09.013.

Doblas, J., Shimabukuro, Y., Sant'Anna, S., Carneiro, A., Aragão, L., Almeida, C., 2020. Optimizing near real-time detection of deforestation on tropical rainforests using sentinel-1 Data. Remote Sens (Basel) 12, 3922. https://doi.org/10.3390/rs12233922.

Doblas, J., Reis, M.S., Belluzzo, A.P., Quadros, C.B., Moraes, D.R.V., Almeida, C.A., Maurano, L.E.P., Carvalho, A.F.A., Sant'Anna, S.J.S., Shimabukuro, Y.E., 2022. DETER-R: An operational near-real time tropical forest disturbance warning system based on sentinel-1 time series analysis. Remote Sens (Basel) 14, 3658. https://doi.org/10.3390/rs14153658.

Doblas, J., Lima, L., Mermoz, S., Bouvet, A., Reiche, J., Watanabe, M., Sant'Anna, S., Shimabukuro, Y., 2022a. Inter-comparison of optical and SAR-based forest disturbance warning systems in the Amazon shows the potential of combined SAR-optical monitoring. Int J Remote Sens (accepted).

ESA, 2012. Sentinel-1: ESA's Radar Observatory Mission for GMES Operational Services, ESA Special Publication. ESA Communications, Noordwijk, The Netherlands.

ESA, 2015. SENTINEL-2 User Handbook. European Space Agency. https://doi.org/GMES-S1OP-EOPG-TN-13-0001.

ESA, 2022. Sentinel-1 Observation Scenario [WWW Document]. URL https://sentinels.copernicus.eu/web/sentinel/missions/sentinel-1/observation-scenario (accessed 7.19.22).

Espírito-Santo, F.D.B., Gloor, M., Keller, M., Malhi, Y., Saatchi, S., Nelson, B., Junior, R.C. O., Pereira, C., Lloyd, J., Frolking, S., Palace, M., Shimabukuro, Y.E., Duarte, V., Mendoza, A.M., López-González, G., Baker, T.R., Feldpausch, T.R., Brienen, R.J.W., Asner, G.P., Boyd, D.S., Phillips, O.L., 2014. Size and frequency of natural forest

disturbances and the Amazon forest carbon balance. Nat Commun 5, 3434. https://doi.org/10.1038/ncomms4434.

Franklin, S.E., Hall, R.J., Moskal, L.M., Maudie, A.J., Lavigne, M.B., 2000. Incorporating texture into classification of forest species composition from airborne multispectral images. Int J Remote Sens 21, 61–79. https://doi.org/10.1080/014311600210993.

Google Earth Engine Team, 2022. Sentinel-1 Algorithms: Pre-processing [WWW Document]. URL https://developers.google.com/earth-engine/guides/sentinel1 (accessed 7.12.22).

Hall-Beyer, M., 2017. Practical guidelines for choosing GLCM textures to use in landscape classification tasks over a range of moderate spatial scales. Int J Remote Sens 38, 1312–1338. https://doi.org/10.1080/01431161.2016.1278314.

Hamunyela, E., Verbesselt, J., Herold, M., 2016. Using spatial context to improve early detection of deforestation from Landsat time series. Remote Sens Environ 172, 126–138. https://doi.org/10.1016/j.rse.2015.11.006.

Hamunyela, E., Reiche, J., Verbesselt, J., Herold, M., 2017. Using Space-Time Features to Improve Detection of Forest Disturbances from Landsat Time Series. Remote Sens (Basel) 9, 515. https://doi.org/10.3390/rs9060515.

Hansen, M.C., Potapov, P.v., Moore, R., Hancher, M., Turubanova, S.A., Tyukavina, A., Thau, D., Stehman, S.v., Goetz, S.J., Loveland, T.R., Kommareddy, A., Egorov, A., Chini, L., Justice, C.O., Townshend, J.R.G., 2013. High-resolution global maps of 21st-century forest cover change. Science 1979 (342), 850–853. https://doi.org/10.1126/science.1244693.

Hansen, M.C., Krylov, A., Tyukavina, A., Potapov, P.v., Turubanova, S., Zutta, B., Ifo, S., Margono, B., Stolle, F., Moore, R., 2016. Humid tropical forest disturbance alerts using Landsat data. Environ. Res. Lett. 11, 034008 https://doi.org/10.1088/1748-9326/11/3/034008.

Haralick, R.M., Shanmugam, K., Dinstein, I., 1973. Textural Features for Image Classification. IEEE Transactions on Systems Science and Cybernetics 4, 610–621.

Hethcoat, M.G., Carreiras, J.M.B., Edwards, D.P., Bryant, R.G., Quegan, S., 2021. Detecting tropical selective logging with C-band SAR data may require a time series approach. Remote Sens Environ 259, 112411. https://doi.org/10.1016/j.rse.2021.112411.

Hirschmugl, M., Deutscher, J., Sobe, C., Bouvet, A., Mermoz, S., Schardt, M., 2020. Use of SAR and optical time series for tropical forest disturbance mapping. Remote Sens (Basel) 12, 727. https://doi.org/10.3390/rs12040727.

Hoekman, D., Kooij, B., Quiñones, M., Vellekoop, S., Carolita, I., Budhiman, S., Arief, R., Roswintiarti, O., 2020. Wide-area near-real-time monitoring of tropical forest degradation and deforestation using sentinel-1. Remote Sens (Basel) 12, 1–32. https://doi.org/10.3390/rs12193263.

Jenicka, S., Suruliandi, A., 2014. A textural approach for land cover classification of remotely sensed image. CSI Transactions on ICT 2, 1–9. https://doi.org/10.1007/s40012-014-0038-4.

Joshi, N., Baumann, M., Ehammer, A., Fensholt, R., Grogan, K., Hostert, P., Jepsen, M.R., Kuemmerle, T., Meyfroidt, P., Mitchard, E.T.A., Reiche, J., Ryan, C.M., Waske, B., 2016. A review of the application of optical and radar remote sensing data fusion to land use mapping and monitoring. Remote Sens (Basel) 8. https://doi.org/10.3390/rs8010070.

Kupidura, P., 2019. The comparison of different methods of texture analysis for their efficacy for land use classification in satellite imagery. Remote Sens (Basel) 11. https://doi.org/10.3390/rs11101233.

Langner, A., Carboni, S., 2021. Forest Degradation Derived by a Newly Developed Sentinel-1 Change Detection Approach, in: 2021 IEEE International Geoscience and Remote Sensing Symposium IGARSS. IEEE, pp. 1019–1022. https://doi.org/10.1109/IGARSS47720.2021.9554574.

Marceau, D.J., Howarth, P.J., Dubois, J.M., Gratton, D.J., 1990. Evaluation of the grey-level Co-occurrence matrix method for land-cover classification using spot imagery. IEEE Trans. Geosci. Remote Sens. 28, 513–519. https://doi.org/10.1109/TGRS.1990.572937.

Mitchell, A.L., Tapley, I., Milne, A.K., Williams, M.L., Zhou, Z.S., Lehmann, E., Caccetta, P., Lowell, K., Held, A., 2014. C- and L-band SAR interoperability: Filling the gaps in continuous forest cover mapping in Tasmania. Remote Sens Environ 155, 58–68. https://doi.org/10.1016/j.rse.2014.02.020.

Moffette, F., Alix-Garcia, J., Shea, K., Pickens, A.H., 2021. The impact of near-real-time deforestation alerts across the tropics. Nat Clim Chang 11, 172–178. https://doi.org/10.1038/s41558-020-00956-w.

Mullissa, A., Vollrath, A., Odongo-Braun, C., Slagter, B., Balling, J., Gou, Y., Gorelick, N., Reiche, J., 2021. Sentinel-1 SAR backscatter analysis ready data preparation in google earth engine. Remote Sens (Basel) 13, 1954. https://doi.org/10.3390/rs13101954.

Negrón-Juárez, R.I., Holm, J.A., Marra, D.M., Rifai, S.W., Riley, W.J., Chambers, J.Q., Koven, C.D., Knox, R.G., McGroddy, M.E., Di Vittorio, A.V., Urquiza-Muñoz, J., Tello-Espinoza, R., Muñoz, W.A., Ribeiro, G.H.P.M., Higuchi, N., 2018. Vulnerability of Amazon forests to storm-driven tree mortality. Environ. Res. Lett. 13, 054021 https://doi.org/10.1088/1748-9326/aabe9f.

Niemi, M., Vauhkonen, J., 2016. Extracting canopy surface texture from airborne laser scanning data for the supervised and unsupervised prediction of area-based forest characteristics. Remote Sens (Basel) 8, 582. https://doi.org/10.3390/rs8070582.

Olofsson, P., Foody, G.M., Herold, M., Stehman, S.V., Woodcock, C.E., Wulder, M.A., 2014. Good practices for estimating area and assessing accuracy of land change. Remote Sens Environ 148, 42–57. https://doi.org/10.1016/j.rse.2014.02.015.

Olofsson, P., Arévalo, P., Espejo, A.B., Green, C., Lindquist, E., McRoberts, R.E., Sanz, M. J., 2020. Mitigating the effects of omission errors on area and area change estimates. Remote Sens Environ 236, 111492. https://doi.org/10.1016/j.rse.2019.111492.

Planet Team, 2022. Planet Application Program Interface: In Space for Life on Earth Online [WWW Document]. URL https://api.planet.com (accessed 7.12.22).

Quegan, S., Yu, J.J., 2001. Filtering of multichannel SAR images. IEEE Trans. Geosci. Remote Sens. 39, 2373–2379. https://doi.org/10.1109/36.964973.

Reiche, J., de Bruin, S., Hoekman, D.H., Verbesselt, J., Herold, M., 2015. A Bayesian Approach to Combine Landsat and ALOS PALSAR Time Series for Near Real-Time Deforestation Detection. Remote Sens (Basel) 7, 4973–4996. https://doi.org/10.3390/rs70504973.

Reiche, J., Hamunyela, E., Verbesselt, J., Hoekman, D., Herold, M., 2018a. Improving near-real time deforestation monitoring in tropical dry forests by combining dense Sentinel-1 time series with Landsat and ALOS-2 PALSAR-2. Remote Sens Environ 204, 147–161. https://doi.org/10.1016/j.rse.2017.10.034.

Reiche, J., Verhoeven, R., Verbesselt, J., Hamunyela, E., Wielaard, N., Herold, M., 2018b. Characterizing tropical forest cover loss using dense sentinel-1 data and active fire alerts. Remote Sens (Basel) 10, 777. https://doi.org/10.3390/rs10050777.

Reiche, J., Mullissa, A., Slagter, B., Gou, Y., Tsendbazar, N.-E., Odongo-Braun, C., Vollrath, A., Weisse, M.J., Stolle, F., Pickens, A., Donchyts, G., Clinton, N., Gorelick, N., Herold, M., 2021. Forest disturbance alerts for the Congo Basin using Sentinel-1. Environ. Res. Lett. 16, 024005 https://doi.org/10.1088/1748-9326/abd0a8.

Sande, M.T., Gosling, W., Correa-Metrio, A., Prado-Junior, J., Poorter, L., Oliveira, R.S., Mazzei, L., Bush, M.B., 2019. A 7000-year history of changing plant trait composition in an Amazonian landscape; the role of humans and climate. Ecol Lett 22, 925–935. https://doi.org/10.1111/ele.13251.

Shimada, M., Itoh, T., Motooka, T., Watanabe, M., Shiraishi, T., Thapa, R., Lucas, R., 2014. New global forest/non-forest maps from ALOS PALSAR data (2007–2010). Remote Sens Environ 155, 13–31. https://doi.org/10.1016/j.rse.2014.04.014.

Song, X., Hansen, M.C., Stephen, V., Peter, V., Tyukavina, A., Vermote, E.F., Townshend, J.R., 2018. Global land change from 1982 to 2016. Nature. https://doi.org/10.1038/s41586-018-0411-9.

Stehman, S.V., 2014. Estimating area and map accuracy for stratified random sampling when the strata are different from the map classes. Int J Remote Sens 35 (13), 4923–4939. https://doi.org/10.1080/01431161.2014.930207.

Stehman, S.V., Wickham, J.D., Smith, J.H., Yang, L., 2003. Thematic accuracy of the 1992 National Land-Cover Data for the eastern United States: Statistical methodology and regional results. Remote Sens Environ 86, 500–516. https://doi.org/10.1016/S0034-4257(03)00128-7.

Sullivan, M.J.P., Talbot, J., Lewis, S.L., Phillips, O.L., Qie, L., Begne, S.K., Chave, J., Cuni-sanchez, A., Hubau, W., Lopez-, G., Miles, L., Monteagudo-mendoza, A., Sonké, B., Doucet, J., Erwin, T.L., Espejo, J.S., Ewango, C.E.N., 2017. Diversity and carbon storage across the tropical forest biome. Sci Rep 1–12. https://doi.org/10.1038/srep39102.

Tso, B., Mather, P.M., 1999. Crop discrimination using multi-temporal SAR imagery. Int J Remote Sens 20, 2443–2460. https://doi.org/10.1080/014311699212119.

Turubanova, S., Potapov, P.v., Tyukavina, A., Hansen, M.C., 2018. Ongoing primary forest loss in Brazil, Democratic Republic of the Congo, and Indonesia. Environ. Res. Lett. 13, 074028 https://doi.org/10.1088/1748-9326/aacd1c.

Tyukavina, A., Hansen, M.C., Potapov, P.V., Stehman, S.V., Smith-Rodriguez, K., Okpa, C., Aguilar, R., 2017. Types and rates of forest disturbance in Brazilian Legal Amazon, 2000–2013. Sci Adv 3. https://doi.org/10.1126/sciadv.1601047.

Tyukavina, A., Hansen, M.C., Potapov, P., Parker, D., Okpa, C., Stehman, S.v., Kommareddy, I., Turubanova, S., 2018. Congo Basin forest loss dominated by increasing smallholder clearing. Sci Adv 4, eaat2993. https://doi.org/10.1126/sciadv.aat2993.

Ulaby, F., Long, D., 2013. Microwave Radar and Radiometric Remote Sensing, unabridged. ed. The University of Michigan Press.

USGS, 2019a. Landsat 8 (L8) Data Users Handbook, USGS Landsat User Services. U.S. Geological Survey.

USGS, 2019b. Landsat 7 (L7) Data Users Handbook, USGS Landsat User Services. U.S. Geological Survey.

Vargas, C., Montalban, J., Leon, A.A., 2019. Early warning tropical forest loss alerts in Peru using Landsat. Environ Res Commun 1, 121002. https://doi.org/10.1088/2515-7620/ab4ec3.

Verhelst, K., Gou, Y., Herold, M., Reiche, J., 2021. Improving forest baseline maps in tropical wetlands using GEDI-based forest height information and sentinel-1. Forests 12, 1374. https://doi.org/10.3390/f12101374.

Vollrath, A., Mullissa, A., Reiche, J., 2020. Angular-based radiometric slope correction for sentinel-1 on google earth engine. Remote Sens (Basel) 12, 1867. https://doi.org/10.3390/rs12111867.

Warner, T., 2011. Kernel-based texture in remote sensing image classification. Geogr Compass 5, 781–798. https://doi.org/10.1111/j.1749-8198.2011.00451.x.

Watanabe, M., Koyama, C.N., Hayashi, M., Nagatani, I., Tadono, T., Shimada, M., 2021. Refined algorithm for forest early warning system with ALOS-2/PALSAR-2 ScanSAR data in tropical forest regions. Remote Sens Environ 265, 112643. https://doi.org/10.1016/j.rse.2021.112643.

Weisse, M.J., Noguerón, R., Vivanco Vicencio, R.E., Castillo Soto, D.A., 2019. Use of near-real-time deforestation alerts: a case study from Peru. World Resources Institute.

Wood, E.M., Pidgeon, A.M., Radeloff, V.C., Keuler, N.S., 2012. Image texture as a remotely sensed measure of vegetation structure. Remote Sens Environ 121, 516–526. https://doi.org/10.1016/j.rse.2012.01.003.

Woodhouse, I.H., 2006. Introduction to Microwave Remote Sensing, 1st ed. CRC Press.

WWF, 2005. Inside the Amazon [WWW Document]. URL https://wwf.panda.org/discover/knowledge_hub/where_we_work/amazon/about_the_amazon/ (accessed 7.12.22).

Ygorra, B., Frappart, F., Wigneron, J.P., Moisy, C., Catry, T., Baup, F., Hamunyela, E., Riazanoff, S., 2021. Monitoring loss of tropical forest cover from Sentinel-1 time-series: A CuSum-based approach. Int. J. Appl. Earth Obs. Geoinf. 103, 102532 https://doi.org/10.1016/j.jag.2021.102532.

Zambrano, J., Cordeiro, N.J., Garzon-Lopez, C., Yeager, L., Fortunel, C., Ndangalasi, H.J., Beckman, N.G., 2020. Investigating the direct and indirect effects of forest fragmentation on plant functional diversity. PLoS One 15, 1–16. https://doi.org/10.1371/journal.pone.0235210.

Zhang, Z., Moore, J.C., 2015. Chapter 4 - Remote Sensing. In: Zhang, Z., Moore, J.C. (Eds.), Mathematical and Physical Fundamentals of Climate Change. Elsevier, Boston, pp. 111–124.

Zimmerman, B.L., Kormos, C.F., 2012. Prospects for Sustainable Logging in Tropical Forests. Bioscience 62, 479–487. https://doi.org/10.1525/bio.2012.62.5.9.